Available online at www.sciencedirect.com
SCIENCE DIRECT®
International Journal of Heat and Mass Transfer 48 (2005) 1000–1016
International Journal of HEAT and MASS TRANSFER
www.elsevier.com/locate/ijhmt

Flow velocities in an experimental kettle reboiler determined by particle image velocimetry

B.M. Burnside *, K.M. Miller [1], D.A. McNeil, T. Bruce [2]

School of Engineering and Physical Science, Heriot-Watt University, Riccarton, Edinburgh, EH14 4AS, UK

Received 11 May 2004
Available online 10 December 2004

Abstract

A particle image velocimetry (PIV) autocorrelation technique was applied to produce whole field vector maps of flow beneath and to the side of a 17 row × 17 column kettle reboiler thin slice rig, boiling pentane at atmospheric pressure. The flow proved to be time dependent. The average values of the mass flowrates of the recirculating liquid were evaluated at various positions and compared to predictions of models of the flow which reproduced the measured pressure drops [B.M. Burnside, K.M. Miller, D.A. McNeil T. Bruce, Heat transfer coefficient distributions in an experimental kettle reboiler thin slice, Trans. IChemE 79A (2001) 445–452]. The use of the results as a platform for 2D numerical modelling of the flow is emphasised.

Keywords: Kettle reboiler; 2-Phase flow; PIV; Heat transfer

1. Introduction

Since convective effects as well as nucleate boiling can have a substantial influence on shell side heat transfer in a kettle reboiler [2–4], knowledge of the flow field is essential. In design, the surface area required for a given heat transfer duty is arrived at by analysing sections along the length of the shell taken at right angles to the bundle axis. On these sections the recirculating flowrate is determined by 1D balances of gravitational, friction and momentum forces, in the two-phase cross-flow within the bundle, against the head of the liquid columns at the sides of the bundle [3,4]. During experiments on 'thin slice' models, thought to reproduce this behaviour, substantial quantities of vapour were washed down at the sides of the bundle by the momentum of the recirculating liquid [5–9]. By observing slowed-down video film of a 241 tube thin slice rig, boiling pentane at 1 atm over a range of heat fluxes from 10 to 50 kW/m^2, Burnside and his colleagues [9] detected also that the flow leaving the bundle at the top was impeded by the geometry of the shell vapour exit to an extent increasing with heat flux. This forced the rising two-phase cross-flow towards the sides of the bundle creating a two-D flow pattern (Fig. 1(a)), and reducing the overall circulation rate and consequently the heat transfer. The arrangement of the vapour outlet corresponding to these flow patterns is shown in Fig. 2. In a previous version of this rig, the vapour outlet from the shell was a 100 mm

* Corresponding author. Tel.: +44 131 449 5111; fax: +44 131 451 3129.
E-mail address: b.m.burnside@hw.ac.uk (B.M. Burnside).
[1] Currently at Aspen Technology Inc./HTFS.
[2] School of Engineering and Electronics, University of Edinburgh.

0017-9310/$ - see front matter © 2004 Elsevier Ltd. All rights reserved.
doi:10.1016/j.ijheatmasstransfer.2004.09.023

Nomenclature

D	diameter, m
Fr	Froude number, $\frac{G}{\rho_l\sqrt{gD}}$
G	mass flux, kg/m^{2}s
g	gravitational acceleration, m/s^2
L	bundle length, m
$\dot{m}$	mass flowrate, kg/s
q	heat flux density, tube outside wall, kW/m^2
Re	Reynolds number
s	tube pitch, m
v	velocity, mm/s
x	mass quality
X_{tt}	Martinelli parameter, $\{\frac{1-x}{x}\}^{0.9}\{\frac{\rho_v}{\rho_l}\}^{0.5}\{\frac{\mu_l}{\mu_v}\}^{0.1}$

Greek symbols

ϵ	void fraction
ϵ_h	void fraction, homogeneous flow
ρ	density, kg/m^3
θ	angle (°)
ϕ_{l0}^2	2-phase friction multiplier, $\frac{\Delta P_{fTP}}{\Delta P_{l0}}$
ΔP_{l0}	pressure drop, liquid flowing alone, Pa

Subscripts

abs	absolute value
feed	feed
h	homogeneous flow
l	liquid
meas	measured
n	normal
recirc	recirculating
x,y	co-ordinate directions

diameter hole followed immediately by a U-bend transition to a 100 mm diameter riser. The rest of the rig configuration was the same [5]. In that case the build-up of two-phase fluid at the top of the shell was much greater, to such an extent that it was impossible to run the rig at heat fluxes much higher than about 20 kW/m^2. Jensen and co-workers boiled R113 at 7 bar in a 13 row half-shell boiler with a 50 mm diameter vapour outlet through the top wall of the shell. At heat fluxes as low as 10 kW/m^2, bubbly re-circulation penetrated down to the 5th row from the bottom of the bundle, with substantial 2D flow in the bundle above this [7]. At 30 kW/m^2 there was virtually no 'liquid only' region at the sides of the bundle and within the bundle boundary the flow direction was horizontally out from the centre or even downwards. On the contrary, Burnside and his colleagues showed by particle tracking techniques [8,10] that there was no evidence of the recirculating liquid entering the bundle from the sides even at heat fluxes as high as 50 kW/m^2. Clearly, the geometry of the shell above the bundle affected flow in the shell fundamentally [9]. Notably, in all the cases surveyed above, the vapour outlet flow area was such that the velocity there was very low, with corresponding negligible pressure drop, even assuming that vapour alone flowed out. Burnside et al. [9] argued that the form of the exit from the shell to the vapour riser and the volume available above the bundle determined the extent of these 2D effects. Obviously, any restriction of the re-circulation will reduce heat transfer coefficients at the tube wall, with consequent under-design using 1D methods [3,4].

The important question arises. Does the phenomenon occur in operating kettle reboilers or does the axial motion of the vapour and the characteristic enlargement of the shell at the vapour outlet preclude it? To answer this question it will be necessary to develop 2D, or even 3D thermo-hydraulic models of kettle reboilers. A good starting point for such modelling is the film and video

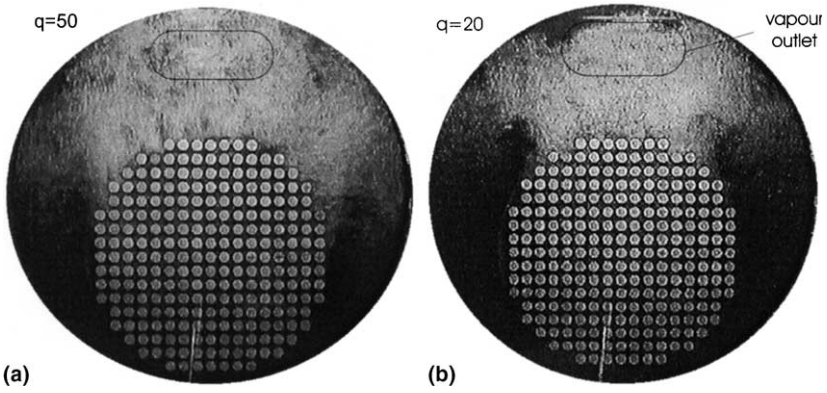

Fig. 1. Boiling pentane at 1 atm [9]. (a) q = 50 kW/m^2; (b) q = 20 kW/m^2.

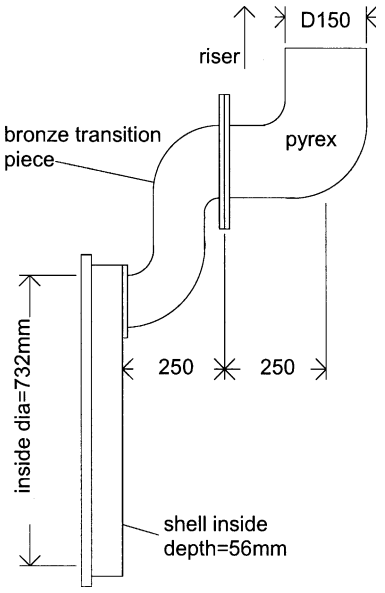

Fig. 2. Vapour outlet arrangement [9].

evidence, pressure drop and heat transfer coefficient data available from existing experimental studies [5,7,8,11]. In addition, the laser Doppler anemometry work of Shire et al. [12] provided velocity measurements in the recirculating stream returning to the bundle at the sides and bottom of the shell. Carlucci et al. [13], Edwards and Jensen [14], Rahman et al. [15] and Burnside [16] have made a start in the direction of 2D modelling. These applications require major changes, for example provision for liquid and vapour in the cells to move in different directions and probably for including the effect of surface tension forces on liquid/vapour separation.

These considerations cast doubt on the direct use of thin slice rig tests in design of kettle reboilers. However, the existence of the data provides an excellent test for further development of CFD techniques to predict the behaviour; techniques which can eventually find their way not only into more precise kettle reboiler design but also into design of many other forms of two-phase heat exchanger. This paper provides further data from a thin slice rig, particularly on velocity distributions determined by Particle Image Velocimetry, a technique new to this area of work.

2. Apparatus

Fig. 1 shows video pictures taken through the toughened glass boiler shell window when boiling *n*-pentane at 1 atm with uniform heat fluxes of $q = 20$ and $50\,\mathrm{kW/m^2}$. Fig. 2 shows the shell/vapour riser bronze casting transition piece which provided a smooth change of cross-sectional area from a $290\,\mathrm{cm^2}$ hole cut in the back wall of the shell to a 150 mm internal diameter pyrex riser. The bundle centre was located 110 mm below the shell centre. It contained 241 19 mm diameter 90Cu:10Ni tubes internally heated by electric resistance cartridge heaters. The tubes were in 17 rows in a 25.4 mm square pitch configuration. Static pressure tappings were disposed in the shell within and without the confines of the bundle [1,9]. The experimental rig flow circuit is shown in Fig. 3. A detailed description is recorded elsewhere [5,8].

The flow circuit has a direct bearing on the flow pattern in the boiler, for example as referred to above, the space available above the bundle and the geometry of the vapour outlet affect the degree of separation of liquid from vapour in the fluid leaving the bundle at the top. Also, the position of the liquid/vapour interface in the boiler depends on a balance of the pressure drop over the boiler and condenser compared to the liquid head of the feed. After condensation in the water cooled condenser and subsequent flowrate measurement, the condensate was collected in a hotwell (Fig. 3). Sufficient head to maintain the interface level in the boiler was obtained by pumping and throttling the feed. Combined de-aeration and gentle boiling occurred in an electrically heated preheater, above which phase separation was effected by a 135° pyrex tee, N. At the higher heat fluxes separation was not complete at this station. A column of two-phase mixture extended from the lower tee, M, to an interface level below separation tee, N. The extra head provided was necessary to effect the higher flowrate as well as changes in head in the shell caused by the increased vapour content therein (Fig. 1). The arrangement of condensers above and below the upper tee and the hotwell, Fig. 3, was required to provide pentane free venting of the system.

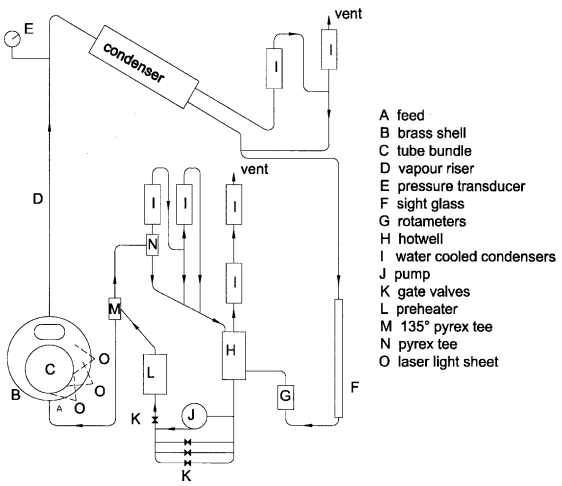

Fig. 3. Test flow circuit.

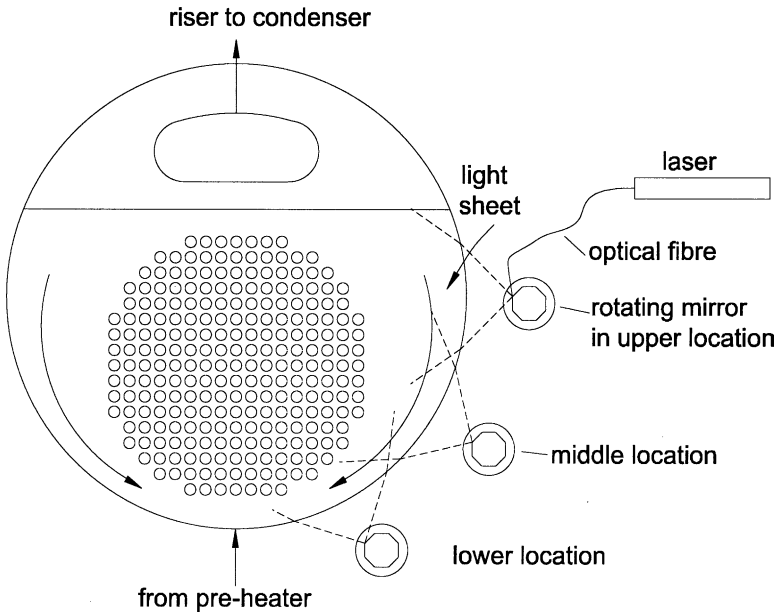

Fig. 4. Schematic of pulsing laser light sheet implementation [8].

The illumination source for the PIV studies was a Spectra-Physics 165 Argon Ion continuous wave laser of 5–7 W output. For safety and space reasons the laser was situated in a room separate from the reboiler. A multi-mode optical fibre delivered the beam to the rig. Fig. 4 is a schematic diagram of the laser light sheet implementation. The scanning beam system comprised an eight facet polygon rotating mirror with an Optical Flow Systems controller capable of giving illumination intervals of between 0.5 and 12.7 ms. The rotating mirror part of the system was bolted to the side wall of the boiler shell at three prepared locations at which perspex windows were located (Fig. 4). It produced a scanning 90° fan of light, 1–2 mm thick when focused. This gave the required pulsing illumination in the plane parallel to the window, situated midway along the length of the bundle. Fluid motion was constrained to be in this plane by the 'thin slice' configuration. All parts of this system within the 'spark free' chamber surrounding the reboiler were totally enclosed. Suitable precautions were taken to prevent eye injury due to inadvertant reflections of laser light through the shell window and the fireproof viewing window in the chamber housing the rig. Details of the control and operation of the system are available elsewhere [8].

The object was to measure liquid phase velocities, so seeding particles were required to follow faithfully the motion of the liquid. The most important factor in guaranteeing this was that the particle density equalled the density of pentane at the normal boiling point, 611 kg/m^3. Further, illumination by the laser light sheet had to be satisfactory. After a thorough survey of commercially available candidates, the silvered 'sherical' particles (SH400 S33) manufactured by Potters Industries were selected for trials. Firstly, a selection of the particles, which contained a range of diameters, was suspended in pentane. This permitted the diameter of the particles neutrally buoyant in the liquid, $D = 20\,\mu m$, to be identified and isolated [8]. Finally, the 20 μm particles were used in a small rig boiling pentane over a single horizontal plain tube identical to those in the rig bundle. These tests confirmed that the illumination properties of the particles were satisfactory. Further, in the presence of the particles, the measured heat transfer coefficients were no different from those measured in their absence.

Images were recorded by a Kodak Megaplus 4.2 digital still image video camera with a resolution of 2000×2000 pixels. Moving pictures were shot using a Panasonic SVHS-C video camera. Velocity vectors were determined from CCD images with the aid of Optical Flow Systems VidPIV software.

3. Experimental procedure and data reduction

The 20 μm seeding particles were added to pentane in a beaker. After boiling conditions had stabilised, the contents of the beaker were poured into the shell through a trap at the top of the vapour riser. A very small amount of seeding was added in the first instance. A process of controlled checking of the quality of the velocity map, followed by small increments to the

seeding, was implemented, until a satisfactory density was achieved. Typically, this varied from 8 to 15 particles/cell. PIV measurements were carried out with the tubes uniformly heated, after each set of readings of pressure drop, liquid and tubewall temperatures had been recorded. Subcooling of the feed entering the shell was less than 1 K based on the pressure at the vapour/liquid interface at the top of the shell. Relative to the saturation temperature corresponding to the pressure at the bottom of the shell the subcooling was 0.75 K greater than this. However, the recirculation rate varied from between 50 and 7× the feed rate as heat flux varied from 10 to 50 kW/m^2. This recirculation, which was at the saturation temperature at the top of the shell, mixed with the feed below the bundle, dominating the temperature of the liquid entering the bundle. As a result, at $q = 10\,\text{kW/m}^2$ the latter was calculated to be only 0.02 K below T_{sat} at the top of the shell, falling to 0.3 K below it at $q = 50\,\text{kW/m}^2$.

The pressure drop and heat transfer data have been reported elsewhere [1,8,9,17]. Preliminary observation was that the presence of vapour bubbles carried downward with the recirculating liquid (Fig. 1), made velocity measurement impossible in the region illuminated by the top window (Fig. 4). Measurements were carried out in the region of the light sheet from the middle window at heat fluxes of 10, 20 and 30 kW/m^2 and in the region lit from the bottom window at all five heat fluxes, 10, 20, 30, 40 and 50 kW/m^2. The laser current was increased in steps of 5 A every 5 min up to the maximum of 35 A giving the maximum light sheet power. Then the laser was allowed to stabilise for at least one hour to minimise beam power variations. Still camera settings suitable for autocorrelation PIV were determined by trial and error, following which a set of images was taken and downloaded to the controlling computer for analysis. Table 1 shows the range of parameters found to be optimal at each test condition.

Table 1
PIV parameters used at different locations and heat fluxes

Heat flux (kW/m^2)	Mirror position	Scan period (ms)	Camera shutter opening period (ms)	No. exposures/ frame
10	Middle	6	20	3
20	Middle	6	20	3
30	Middle	6	20	3
10	Lower	6	20	3
20	Lower	6	20	3
30	Lower	4	20	5
40	Lower	3	20	6
50	Lower	3	20	6

As an example, Fig. 5(a) and (b) show digital photographs taken with illumination through the lower and middle windows at $q = 10\,\text{kW/m}^2$. It was difficult to fit the delivery lens and optical fibre/rotating mirror into the space available close to the shell. As a result there was a reflection off the delivery lens. This caused a double reflection to appear in the recorded images, making it impossible to determine vectors where it occurred. The areas affected are seen as gaps in the vector maps obtained, see particularly, Fig. 7(a) and (c) and Fig. 8(a)–(d).

3.1. Velocity vector maps from digital photographs

3.1.1. Basic principles

The basic principle of PIV is simple [18]. The tracer particles in the flow are illuminated and their positions

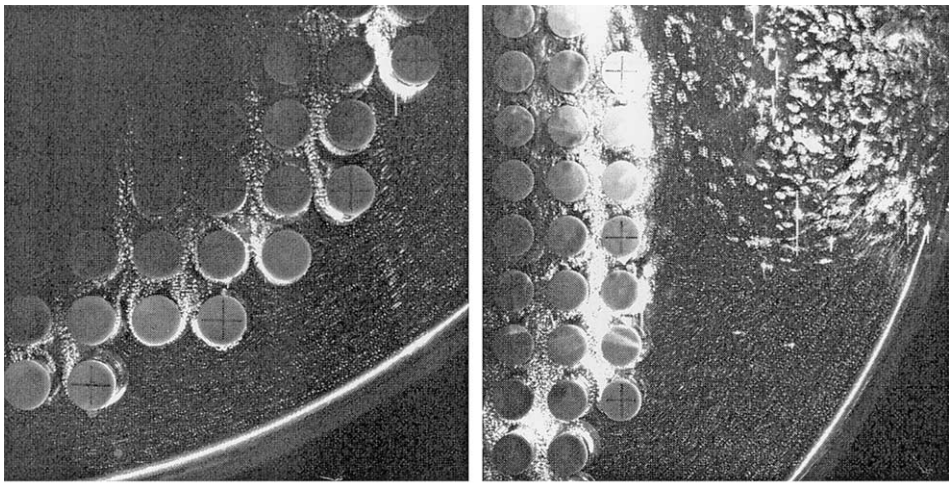

Fig. 5. Digital photographs taken at $q = 10\,\text{kW/m}^2$ (a) illumination through lower window; (b) through middle window.

recorded by digital photography at two successive instants. The photographic 'flow record' of the whole 2D field is then divided into a grid of cells. In each cell, the distance moved by the tracer particles from the time of the first image being recorded to the second is determined. Knowing this distance travelled and the time taken, the velocity of the flow in that cell is known. This is done for every cell, each cell yielding one velocity vector, leading to a 2D vector map of the 'instantaneous' velocity field at the time of recording. At the time the reported work was carried out, the usual approach was to illuminate the flow stroboscopically, here using a scanning laser beam, and to record a double- or multiple-exposure photograph of the flow. The camera shutter was held open long enough so that each tracer particle was illuminated twice or more often and therefore gave at least a pair of images on the flow record. This was PIV using the 'autocorrelation method'.

In the alternative 'cross-correlation method' the complication of arranging for stroboscopic illumination be avoided by exposing the first and second images as successive frames recorded by the digital camera. The movement of the tracer particle images over the time between the exposure of the first frame and the second can then be analysed to give the velocity map. Cross-correlation has a number of significant advantages over autocorrelation. However, at the time of these tests, the 2000×2000 pixels resolution of the digital camera employed was exceptional. The cross-correlation cameras available then offered resolution which would have been at best marginal for this application and would have degraded the quality of the velocity maps. This ruled out use of the cross-correlation method.

3.1.2. Implementation

For the lower window illumination, the magnification factor of the original image was estimated to be 0.0972 ± 0.0003 mm/pixel; 0.1146 ± 0.0005 mm/pixel for middle window lighting. These figures were based on photographs taken in the absence of boiling. An interrogation cell size of 64×64 pixels was selected, corresponding to 6.2×6.2 mm in the model boiler. In order to maximise the data throughput (i.e. minimise the chances of a cell being devoid of any tracer images) in what were quite challenging conditions, the cells were overlapped, having centres separated by 32 pixels, or 3.1 mm. The analysis of the digitised images was the evaluation of the auto-correlation function for each interrogation area. The location of symmetrical peaks in the auto-correlation plane gave the local mean particle displacement between successive illumination pulses. Optical Flow systems ViPIV software was used to evaluate a Fast Fourier version of the auto-correlation function and the velocity vectors.

If the tracer particle density had been uniform, every interrogation cell could be analysed satisfactorily to give a velocity vector. No overlap would be necessary. This was not the case. Overlapping gave the same result as a simple interpolation between the centres of neighbouring, non-overlapped cells. With less than easy conditions to guarantee a suitable concentration of tracer particles in any given cell, the chances of getting adequate conditions is improved by using more cells/unit area, hence overlapping. The factors resulting in the difficulty of ensuring a suitably uniform tracer concentration are obvious. The flow was highly complex with vortices, eddies and highly sheared areas, all of which tended to affect the distribution of tracer particles. Further, the presence of vapour bubbles, occupying more and more of the field as heat flux increased meant that getting an interrogation cell which was not bubble dominated became increasingly difficult. Trying more cell locations by overlapping increased the chances of obtaining vectors in these areas.

The vectors obtained from the PIV software had to be checked visually. This involved ensuring that the velocity obtained matched the original motion of the seeding. Video footage was used to determine the direction of the velocity in cases where the ambiguity could not be resolved by inspection of the overall flow characteristics. Vectors found not to correspond to the particle traces were removed.

3.2. Errors

Individual errors in velocity arrived at from the autocorrelation analysis originate from a number of sources [18]. Typically based on Monte Carlo simulations of PIV analysis, factors contributing to the errors can be identified and their magnitudes estimated.

An implicit assumption for PIV analysis is that the flow is uniform over each interrogation cell. Clearly, this cannot be so for any flow of interest. The flow studied here is a case in point. Referring to Fig. 13 the largest variation of velocity from cell-to-cell was no more than 10%. For the conditions obtaining this gives a resultant error of approximately ± 2 pixels and a velocity error of no greater than 10% of the largest velocities, ± 0.04 m/s [18]. More typical cell-to-cell variations of about 5% give much smaller errors of about ± 0.5 pixels, ± 0.01 m/s.

Simulations show that the random error in the measured particle image displacement, and thus in the velocity, does not vary greatly over a wide range of displacements [18]. For autocorrelation, the very smallest displacements of less than about one particle image diameter, may not give a measurable velocity. For all larger displacements, this error may be estimated at between 0.015 and 0.025 pixels for this application. This is insignificant when compared to the velocity gradient errors above.

Particle image diameters were about 2 pixels in this study, which is close to the optimum diameter of 1.5

pixels suggested by simulations [18]. This suggests an error in the range 0.05–0.1 pixels for the analysis method using 64×64 pixels/interrogation area. Again this is insignificant compared to the velocity gradient errors.

While noise has not been quantified for the images presented, even with 50% noise, that is half of the images not forming part of a correlated pair, the error in velocity is only 0.1 pixels. Therefore, it is thought unlikely that the measured velocities were badly affected by noise.

The fact that the flow is not fully two-dimensional will cause cases to arise where a tracer particle is not moving in a plane exactly parallel to the plane of the camera detector array. This produces a small negative bias on the measured velocities. However, this is expected to amount to something of the order of 0.01 pixels and was not a significant source of error for this study.

Thus the errors in the magnitude of velocity were due mainly to velocity gradients in the flow. They amount to a maximum of ±10% at the highest velocities with an average of about ±5%. While a more detailed analysis of errors in individual velocity vectors could be attempted, the velocity gradients across each interrogation cell varied over the measured area and the number of particle image pairs also varied somewhat. So it is impossible to assign a single absolute error. Rather, the preferred approach here is a mass balance check, Section 4.1, which demonstrated that the errors were indeed well under control.

The errors in velocity, ϵ_v, correspond to errors ϵ_θ in flow direction θ (Fig. 6). In this figure the solid line is the best-guess vector and the dotted line is the worst-case, the circle representing ϵ_v. This gives an absolute error in direction of $\epsilon_\theta = \frac{\epsilon_v}{v}$. Typically for velocities of 300 mm/s, $\epsilon_v = \pm 15$ mm/s which gives an error of about ±3° in direction.

3.3. Calculation of mass flux and mass flowrates

Average mass fluxes across boundaries were determined by fitting polynomial curves to the normal components, v_n of the velocity and integrating $G_n = \rho_l v_n$ over the boundary, Eq. (1),

$$\overline{G}_n = \frac{1}{A}\int_0^A G_n \, \mathrm{d}A \tag{1}$$

where A is the area of the boundary. Mass flowrates were determined as the product $\overline{G}_n A$.

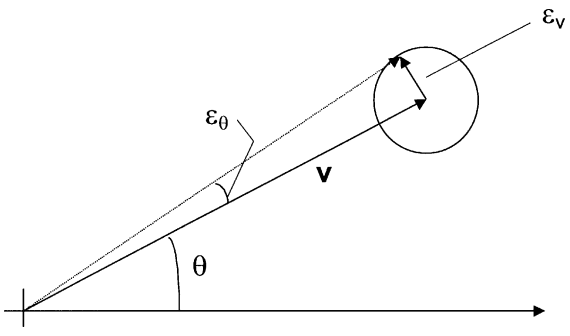

Fig. 6. Velocity direction error.

4. Results

Examples of the vector maps derived from the digital photographs are shown in Figs. 7–9. The origins of coordinates in the figures are the tubes marked with a cross. The +ve direction of the x-axis is from left to right and of the y-axis from bottom to top. The scale of the vectors is indicated in the figure captions in units of velocity/unit length on the coordinate scales. Full size versions of these maps are available [8].

Before discussing the results, two questions relating to accuracy of PIV measurements must be answered. How accurately was mass conserved based on the velocity vector maps and was time variation of the flow an important factor?

4.1. Mass balance check

To check the estimate of errors in the velocities, Section 3.2, mass balances were determined at 10, 20, 30, 40 and 50 kW/m^2. These were based on the integrated normal components of velocity, Eq. (1), along the boundaries into and out of the three control volumes shown in Fig. 10. Table 2 shows the results. The lengths of the sides of the control areas are given in the captions to Fig. 10. The lines defining the control areas were drawn between vector rows and columns, and the average of the vectors immediately either side of the line taken. For area 1, Fig. 10(a), there were seven pairs of vectors along each edge. For area 2, there were eight pairs of vectors along the top and bottom and seven along the left and right edges. For area 3, Fig. 10(b) there were nine pairs along top and bottom and 10 along the left and right boundaries.

The mass balance errors, defined by Eq. (2), were all less than 10% and in many cases a lot better.

$$\text{error}\% = \left|\frac{\dot{m}_{\text{out}} - \dot{m}_{\text{in}}}{\dot{m}_{\text{out}}}\right| \times 100 \tag{2}$$

Based on this evidence it was inferred that the errors in velocity estimated in Section 3.2 were confirmed.

4.2. Flow oscillation

Time variation of the flow was another factor affecting the accuracy of determination of velocity and mass flux. The two-phase mixture above the bundle oscillated

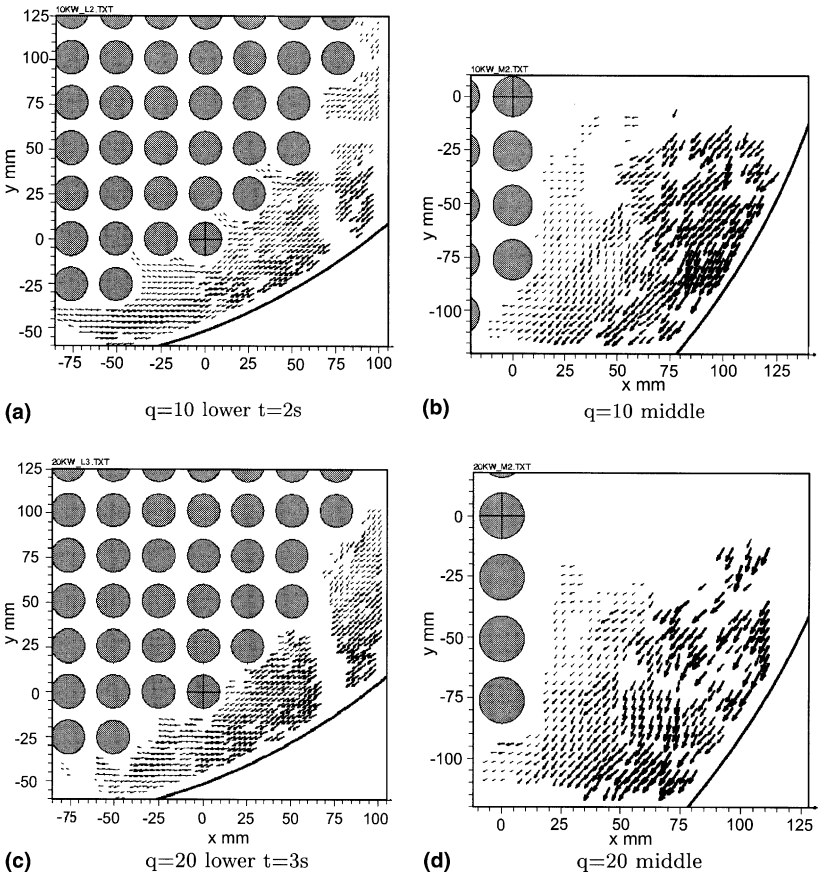

Fig. 7. Vector maps middle and lower window illumination q =10 and 20 kW/m^2 (vector length scale: 200 mm/s ≡ 2.6 mm on the coordinate scales).

from side to side with a typical time period of 2–5 s. As a result, the bubble entrapment vortex, Figs. 1 and 11, moved up and down in the same time period. This was accompanied by a periodic variation in the recirculation velocity, posing a problem for the PIV measurements. The effect varied with heat flux.

At all five heat fluxes a time series of five images was taken at one second intervals. This was the minimum interval required to download each image to the computer and reset the camera for the next shot. Vector maps were calculated for each of these images. The mass flow rates across a vertical plane, situated immediately below the centre line of the marked reference tube in row 2, column 14 of the bundle, Fig. 10 and extending from close to the reference tube wall to close to the shell wall, were calculated for each image as described in Section 3.3. It was not possible to extend the plane to these extremities because of the lack of suitable particle images there. Of the five available velocity vector plots at each heat flux, the one with mass flow rate nearest to the average value was taken to represent the average behaviour and used in all subsequent calculations. These are the vector maps depicted in Fig. 7(a) and (c) and Fig. 8(a) and (c), where the image source is identified. For example, this occurred at $t = 2$ s at $q = 30$ kW/m^2, the corresponding vector map being Fig. 8(a). Table 3 shows the results.

The percentage value of the amplitude relates to the average mass flow rate of the five used in each case. The deviation quoted is the difference between the average of the five values obtained and the value chosen to be the average. Since the maximum estimated error in the velocities, based on a given vector map, averaged about ±5% (see Section 3.2), obviously oscillations in the recirculating flow are a major factor in determining mass flowrates at all heat fluxes. The deviation of the average plot chosen from the true average is small when compared to the error in calculating these values. The vector maps presented in Figs. 7 and 8 are those representing the average velocity condition referred to above. These were the ones used subsequently to calculate the mass flowrates. Notably, the fluctuations in velocity at 30 and 50 kW/m^2 appeared to be greater than at 40 kW/m^2. This seems odd. It is possible that at

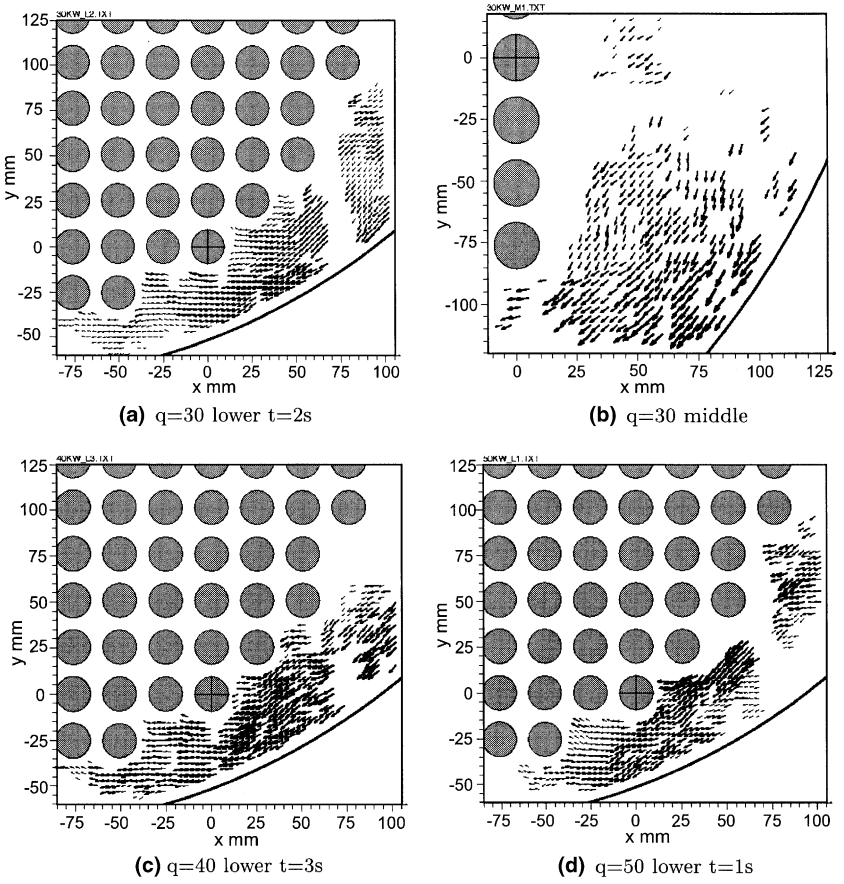

Fig. 8. Vector maps middle and lower window illumination q =30, 40 and 50 kW/m^2 (vector length scale: 200 mm/s ≡ 2.6 mm on the coordinate scales).

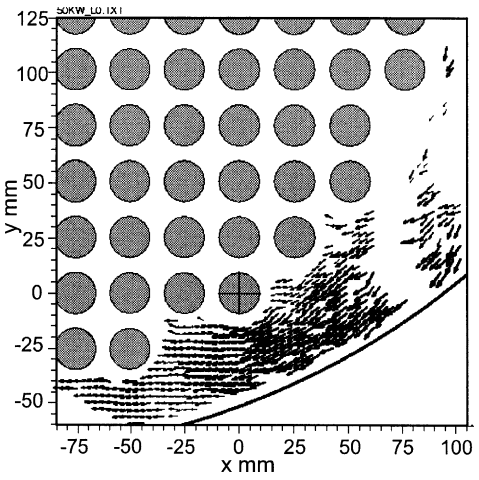

Fig. 9. Vector map lower window illumination, $t = 0$ s, $q = 50$ kW/m^2 (vector length scale: 200 mm/s ≡ 2.6 mm on the coordinate scales.

40 kW/m^2 peaks, higher than those detected, occurred in the 1 s intervals between shooting the video images. The peak mass flowrate through the chosen boundary occurred at 40 kW/m^2, Table 3.

4.3. Images-out-of-phase errors

PIV measurements with illumination through the lower and middle windows were made necessarily at different times. Thus, due to the flow oscillation, there is a further error if these velocity measurements are compared. The level of this error is indicated by the amplitude of the oscillations, Table 3. It is particularly high at q = 30 and 50 kW/m^2. To provide a further check on continuity, mass balances at q = 10, 20 and 30 kW/m^2, carried out across the planes *ab* and *ac*, Fig. 12(a)–(c) are shown in Table 4. These planes and the shell wall form an enclosed space. Since the fluid is almost entirely liquid in this region, continuity dictates that inlet and

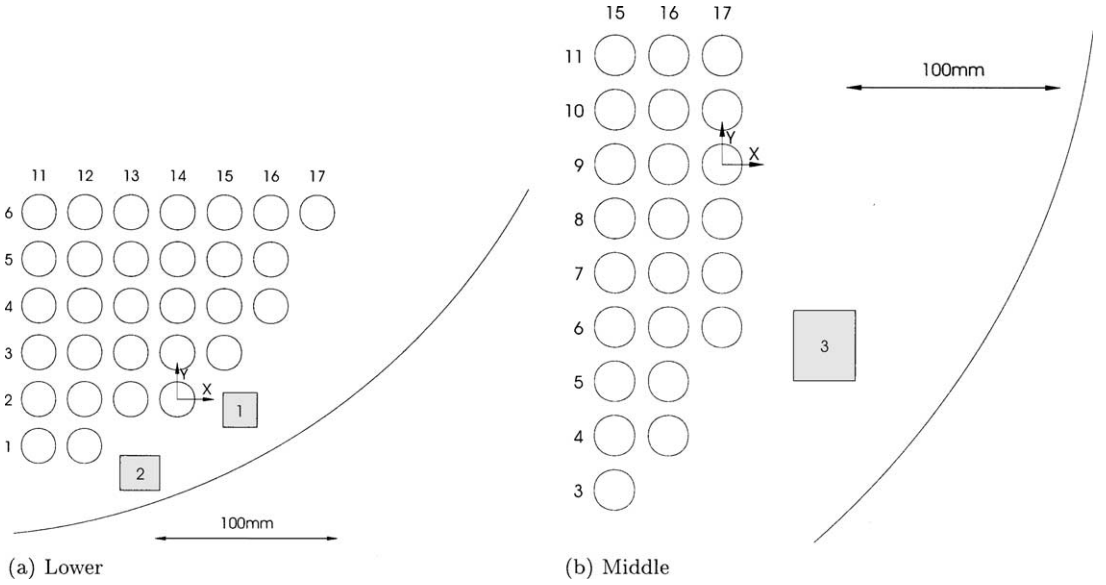

Fig. 10. Mass balance check: control volume size: (a) 18.6 × 18.6 mm; (b) 21.8 × 18.7 mm; (c) 29.3 × 33 mm.

Table 2
Mass balance errors

Heat flux (kW/m^2)	Area	$\dot{m}_{in}$ (kg/s)	$\dot{m}_{out}$ (kg/s)	Error (%)
10	1	0.176	0.165	6.7
10	2	0.158	0.155	1.9
10	3	0.291	0.290	0.3
20	1	0.219	0.217	0.9
20	3	0.323	0.346	6.6
30	1	0.228	0.221	3.2
30	3	0.356	0.332	7.2
40	1	0.347	0.348	0.3
50	1	0.270	0.246	9.8

outlet flowrates measured at any given time, should be the same. The balance was satisfactory at 10 and 20 kW/m^2 considering that the images used to evaluate the velocities were inevitably out of phase. At 30 kW/m^2, however, as referred to above, Table 3 and Fig. 11, the amplitude of the time variation of the flow was high and the error consequently greater.

4.4. Test planes for mass flux determination

In addition to planes *ab* and *ac*, Fig. 12 shows a series of horizontal and vertical planes across which mass fluxes were calculated. The positions of these planes, and the proximity of their extremities to the shell wall and the bundle, were limited by the availability of sufficient vectors to ensure that accurate velocity profiles were obtained. As far as was possible, the planes were located in similar positions at each heat flux. Typical profiles are shown in Fig. 13.

5. Discussion

As expected, the recirculating liquid flow at the side of the bundle followed the contour of the shell wall (Figs. 7 and 8). The flow was well into the turbulent region at all heat fluxes, $Re \approx 52\,000$ at 200 mm/s. This was based on the equivalent diameter of the horizontal flow cross-section between the bundle edge and the shell wall, level with row 7. Fig. 13(a) and (b) show the profiles of velocity, v_{abs}, at q = 10 and 20 kW/m^2 level with rows 5–7 and the flow inclination to the horizontal, θ, defined in the figures. In Fig. 13, the origin of x is the centre of the tube in row 2, column 14 of the bundle, marked in Fig. 12. The origin of y is at the centre of the tube in row 9, column 17, also marked in Fig. 12. Images with sufficiently well illuminated particle tracks became more difficult to obtain as heat flux was raised with increasing vapour content. The exaggerated saw tooth nature of the velocity profiles (Fig. 13(a) and (b)) reflects this. Across the planes, level with rows 6 and 7, θ, controlled by the shape of the shell wall, was generally between 45° and 80°, but decreased near the bundle (low x) because of the shearing effect of the two-phase stream of fluid rising up the outside column of tubes (Figs. 5(b) and 11). What evidence was available suggested that very little liquid entered the bundle at the sides above row 5. Indeed at q = 30 kW/m^2, this was prevented by the strongly rising two-phase fluid stream as is evident from the digital photographs (Fig. 11).

At the side of the bundle, the velocity near the shell wall was highest falling to its lowest value near the bundle in the presence of the upward two-phase stream. Thus, at 10 kW/m^2, Fig. 13(a), v_{abs} fell from

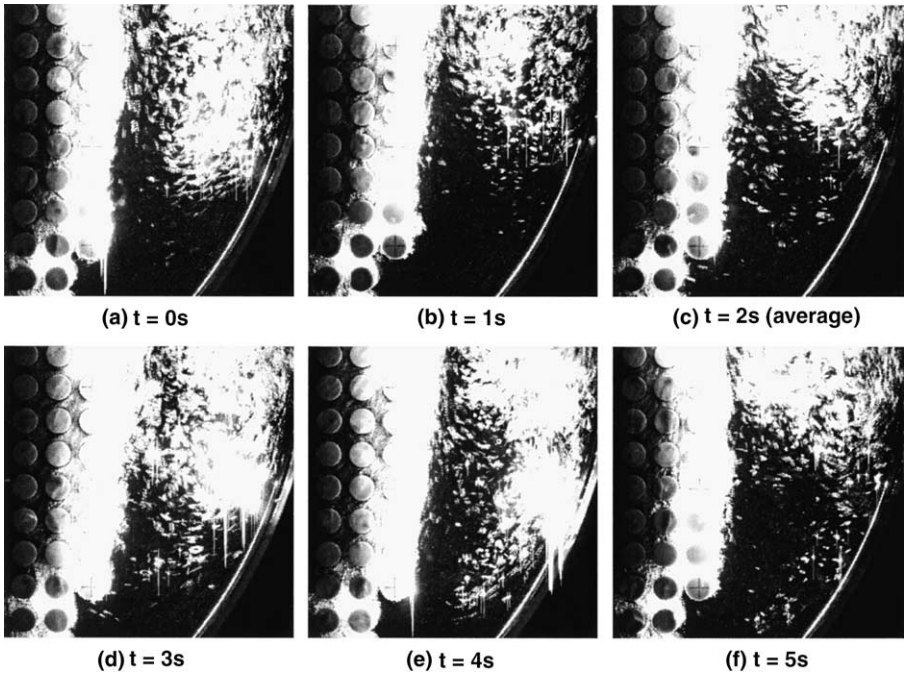

Fig. 11. Oscillating bubble entrapment vortex. Middle mirror lighting ($q = 30\,kW/m^2$).

Table 3
Mass flux through test plane based on vector map nearest the average, with amplitude and deviation from the average mass flux

Heat flux (kW/m^2)	Amplitude		Average (kg/s)	Deviation	
	(kg/s)	%		(kg/s)	%
10	±0.021	±13	0.158	0	0
20	±0.025	±11	0.222	0.012	5
30	±0.050	±24	0.207	0.005	2
40	±0.040	±14	0.289	0.008	3
50	±0.065	±28	0.235	0	0

350–400 mm/s at the wall to 100–130 mm/s near the bundle, level with rows 6 and 7. Level with row 5, it fell from 400 mm/s to 80 mm/s. At $20\,kW/m^2$ the behaviour was similar with v_{abs} falling from 400 to 80 mm/s at row 6 and 7 level and from 400–100 mm/s opposite row 5 (Fig. 13(b)).

At the bottom of the shell, at all heat fluxes, liquid flowed into the bundle through all of the gaps between columns 12 and 17 (Figs. 7(a) and (c) and 8(a)–(d)). Nearer the bundle centre line, where the feed entered free of seeding particles, the flow pattern was less clear because there were insufficient particle traces to determine reliable velocities. On all the vector maps, below the gap between columns 16 and 17, there was a region where velocities could not be determined because of the light reflection from the delivery lens. Examples of the profiles of flow velocity and direction across the vertical planes immediately below columns 13, 14, 15 and 16, are shown in Fig. 13(c) and (d) at 20 and $50\,kW/m^2$.

At $20\,kW/m^2$, below columns 16 and 17 the flow angle θ increased upwards due to the relatively steeper slope of the bundle outline than the shell wall (Figs. 7(c) and 13(c)). Further in, below columns 12, 13 and 14 the angle decreased upwards due to up-take by the bundle. Below column 17, v_{abs} first falls from 250 mm/s near the bundle to 150 mm/s further out, before rising again to 350 mm/s near the shell wall. The reason for this local minimum is not clear. Perhaps the higher value near the tubes was caused by acceleration due to the suction effect of the bundle. The profile of v_{abs} was similar below column 16. Although there is a drop in flow area between the planes below columns 15 and 14 and between 13 and 12, there is a fall in v_{abs} in the former case and no change in the latter. Obviously the up-take by the bundle reduced the mass flowrate. v_{abs} was in the range 175–250 mm/s in this region. Below columns 12–14, the flow direction is practically horizontal near the shell wall but directed upwards as the liquid flowed into the bundle.

At $q = 50\,kW/m^2$, Figs. 8(d) and 13(d), below column 16 and to a lesser extent column 15, there was a region of low velocity, ≈250 mm/s compared to ≈400 mm/s elsewhere. This phenomenon was not observed at any of the lower heat fluxes. A possible cause may be the much greater effect of suction towards the centre at the bottom of the bundle on the flow near the bundle. Moreover, the

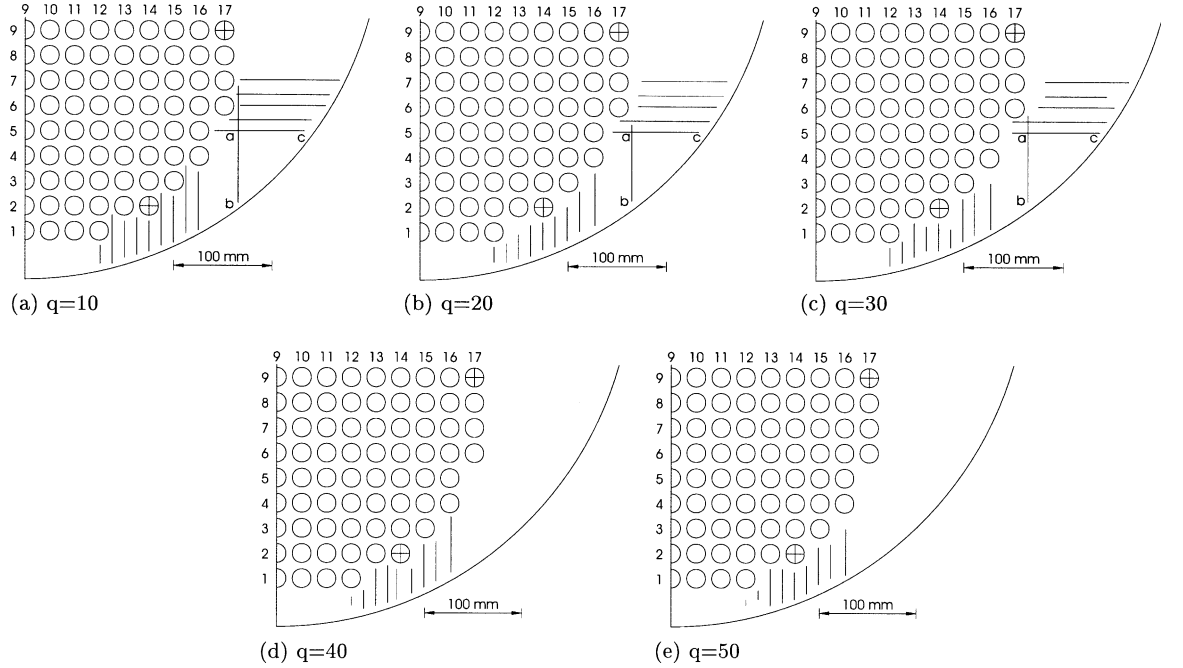

Fig. 12. Position of planes for mass flux evaluation.

Table 4
Mass balance across planes *ab* and *ac*, Fig. 12

Heat flux (kW/m^2)	$\dot{m}_{ab}$ (kg/s)	$\dot{m}_{ac}$ (kg/s)	Balance (%)
10	0.485	0.444	−2
20	0.552	0.654	−16
30	0.397	0.575	−31

oscillating motion of the separation vortex and the liquid–vapour interface at the top of the shell imposed an oscillation on the descending recirculation. Because of the greater suction near the bundle, this effect influenced the liquid mainly near the shell wall. Thus a temporal variation of the profiles occurred, with the maximum amplitude near the shell wall. On this argument the video image, on which Fig. 9 was based, was taken when the interface and vortex were in the rising part of the cycle. This temporal variation is confirmed by the vector map shown in Fig. 9 which was derived from a video image taken 1 second before. In this map there is no region of low velocity near the shell wall. The main flow, Fig. 13(d) was inclined at 50° to the vertical below column 16 falling to 30° below columns 15 and 14. Below column 13, the main flow was horizontal, with an element flowing upwards at about 30° into the bundle. Noticeably, the velocity near the bundle fell progressively from below column 15 to below column 13. The effect of up-take by the bundle is obvious.

In this work the peak-to-peak mass fluxes amounted to over 25% of the average flowrate, Table 3, even at $q = 10\,\mathrm{kW/m^2}$ when no difficulty was experienced with liquid–vapour disengagement and thin slice conditions were closest to those in the commercial unit. The flow oscillation could be observed clearly on the video images. This suggests that it may be prudent to carry out a 3D time dependent analysis as an adjunct to kettle reboiler design. The effect of perturbations, for example in inlet flowrate, composition or overall pressure drop may then be explored. In the commercial unit, these may result in the liquid/vapour interface 'slopping' from side to side and possibly, even from end to end of the shell, causing oscillation of the separation vortices at the sides of the bundle. Changes in the interface level also alter the pressure at the bottom of the bundle. Both of these factors, velocity and pressure fluctuation, affect the void fraction which in turn affects the flow resistance in the bundle columns and hence the recirculation velocity and the interface level itself. For example, at the low point of the velocity cycle, corresponding roughly to the maximum interface level and the maximum hydraulic pressure, the void fraction falls due to the pressure increase but rises in the bundle columns due to the reduction in velocity. The first of these effects is stable, because it tends to decrease flow resistance and hence increase flowrate again. The second is unstable, since increase in void fraction increases flow resistance and tends to reduce velocity further. In addition, flow and heat transfer are coupled due to the usual in-tube condensing fluid heating, unlike the uniform heat flux employed in this work. Clearly, the factors above are

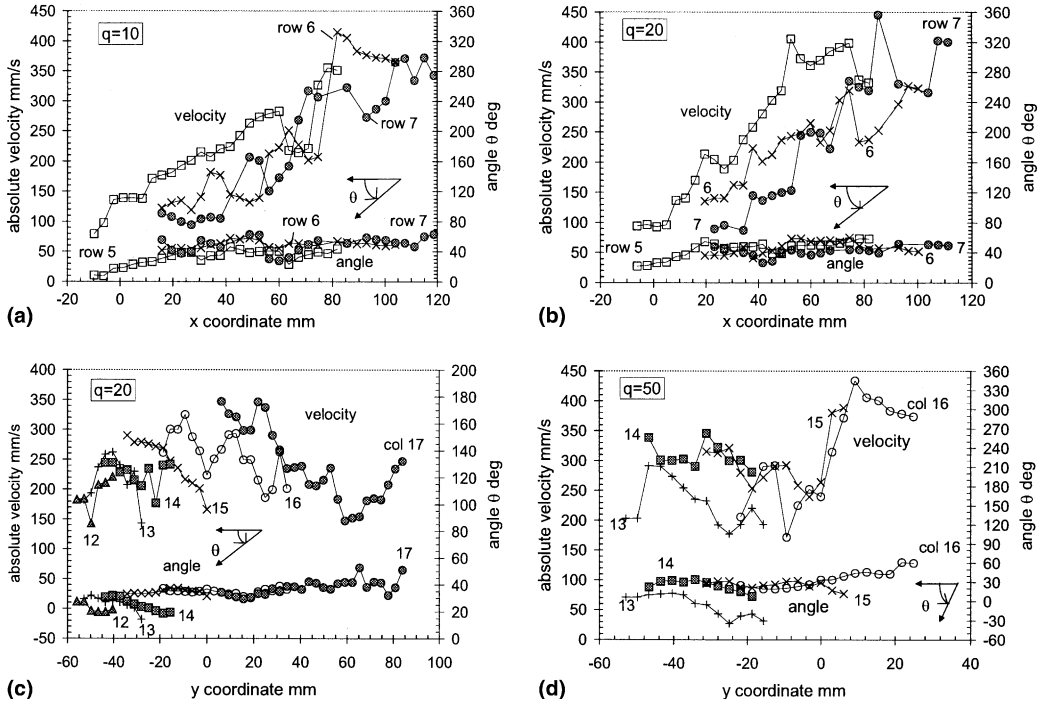

Fig. 13. Profiles of velocity and angle around bundle, row and column numbers identified across horizontal planes. (a) q =10 kW/m^2; (b) q =20 kW/m^2; across vertical planes, (c) q =20 kW/m^2 and (d) q =50 kW/m^2.

important in design, particularly in the calculation of maximum heat flux.

5.1. Mass flowrates

As stated above, the calculating plane lengths were limited to avoid areas near the tubes and the shell wall where the images did not allow velocities to be determined, particularly at the higher heat fluxes. To mitigate the distorting effect of this on the mass flowrates between shell and bundle, the components of mass flux, G_x and G_y normal to the planes shown in Fig. 12 were fitted by least squares. The fits were integrated, Eq. (1), over the whole area between shell wall and the cylinder circumscribing the bundle, centre the tube in the 9th row and 9th column, radius 231.2 mm, to obtain the mass flowrates, $\dot{m}_x$ and $\dot{m}_y$. The values obtained are plotted in Fig. 14. Within the experimental error of 10% and allowing for indeterminate errors in extrapolating mass fluxes to the boundaries, $\dot{m}_y \approx 0.7$ kg/s at all three heat fluxes from the 7th down to the 6th row level (Fig. 14(a)). This confirms observations of particle traces which showed that no liquid enters the bundle at this level [10]. Below this, at q = 10 and 30 kW/m^2, there is a noticeable drop in $\dot{m}_y$ but not at 20 kW/m^2. Presumably at 10 kW/m^2 the repelling effect of the two-phase mixture rising up the outside column of tubes is at a minimum, permitting easier penetration of liquid into the bundle than at 20 kW/m^2. At 30 kW/m^2 the swirling effect of the rotating vortex is greater than at 20 kW/m^2, causing greater entrainment of liquid into the strongly rising two-phase flow. Indeed, the horizontal component of the velocity on the planes 5–7 is higher at 30 kW/m^2 than at the other heat fluxes.

Below the bundle, $\dot{m}_x$ through the extended surface *ab*, Fig. 12, is 0.58, 0.68 and 0.60 kg/s at q = 10, 20 and 30 kW/m^2. Through the extended planes level with row 7 $\dot{m}_y$ = 0.52, 0.68 and 0.54 kg/s at corresponding heat fluxes (Fig. 14). Thus, within experimental error, no more than a very small amount of liquid flows into the bundle. The up-take of liquid by the bundle, as the flow is drawn into the gap below it, results in the more or less constant rate of decrease of flowrate observed across to column 14 at 10 and 20 kW/m^2, and to column 12 at 40 and 50 kW/m^2 (Fig. 14(a)). The saw tooth form of the $\dot{m}$ variation in the figure is the result of accumulated errors in velocity measurement and extrapolation of the planes. The curves show virtually no up-take by the bundle between the columns 14–12 for q = 10–30 kW/m^2. The error in extrapolating the measured velocities is particularly high here where the measurement planes are short. Also, there is the influence of the feed flow through the 28 mm diameter ports, one of which is situated below column 11. A further influence may be the downward acceleration of the flow into the gaps between columns 12 and 14 and the shell wall.

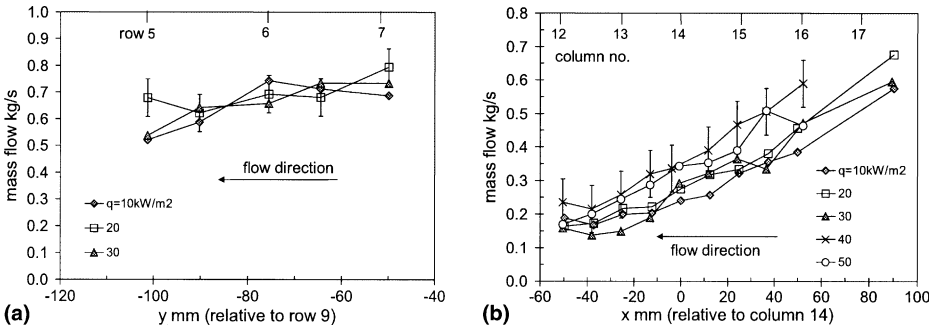

Fig. 14. Mass flowrates across planes designated in Fig. 12. (a) Beside bundle, $\dot{m}_y$; (b) below bundle, $\dot{m}_x$ (10% error bars shown).

5.2. Comparison with predicted recirculation rates

The recirculation rate, m_{recirc}, was predicted by a 1D model [4,1] of the bundle. The value of $G_{\min}$ for which the sum of the gravitational, frictional and momentum pressure drops balanced the liquid head at the side of the bundle was determined making the following assumptions:

1. Ratio of void fraction, ϵ to the homogeneous flow value, ϵ_h, given by the Schrage et al. [19] correlation, Eq. (3)

$$\frac{\epsilon}{\epsilon_h} = 1 + 0.123 Fr^{-0.191} \ln x \tag{3}$$

   Since Eq. (3) was developed from air/water and boiling R113 cross-flow measurements, the alternative Premoli, CISE pipe flow correlation [20], based on a diameter equivalent to the mean of $A_{\min}$ and $A_{\max}$, was used for comparison.
2. Ishihara correlation [21], Eq. (4), for the two-phase friction multiplier, ψ_{l0}^2,

$$\psi_{l0}^2 = 1 + \frac{8}{X_{tt}} + \frac{1}{X_{tt}^2} \tag{4}$$

3. Single phase pressure drop ΔP_{l0} from ESDU 79034 [22].

The measured and predicted pressure drops and mass fluxes at 10 and 50 kW/m^2 are compared in Fig. 15. At the lower heat flux no lateral flow was observed in the flow over the tubes and the vapour content of the liquid at the sides of the bundle was low, indicating 1D conditions [9]. At 50 kW/m^2, lateral flow was observed above the third row and void fraction at the sides was substantial above row 10, Fig. 1(b)—very much 2D conditions. The ordinates in Fig. 15 are the 2-row pressure drops. Predicted mass fluxes shown, $G_{\min}$, are the recirculation values, that is the predicted minimum mass flux through the bundle less the feed mass flux. At 10 kW/m^2 the measured recirculation mass flowrate, $\dot{m}_{\text{circ}}$, was taken to be that crossing the horizontal plane adjacent to row 6, 0.7 kg/s (Fig. 14(a)). This was referred to $A_{\max}$ of half the bundle columns to obtain the measured value, $G_{\min}$, shown in Fig. 15(a). At 50 kW/m^2 $\dot{m}_{\text{circ}}$ was taken to be 0.5 kg/s flowing through the vertical plane below column 16 (Fig. 14(b)). Since this omitted the recirculation between columns 16 and 17, the measured value of $G_{\min}$ shown was referred to half the bundle of 15 columns.

The 1D model predicts pressure drop and mass flux data excellently at 10 kW/m^2 using both void fraction correlations (Fig. 15(a)). Predicted minimum mass flux, $G_{\min}$ = 54.0 kg/m^{2}s using Eq. (3) compared to 57.9 kg/m^{2}s measured, a 7% underprediction. Based on the Premoli equation void fraction, $G_{\min}$ = 78.1 kg/m^{2}s, a 35% overprediction. In view of this the former correlation was used subsequently. At 50 kW/m^2, the 1D model predicts a rising trend of ΔP with height while the data shows a fall, resulting in a prediction 2.5× the measured value at the top of the bundle (Fig. 15(b)). The fall is due to a reduction in flowrate up the columns due to lateral flow accompanied by a reduction in the driving head at the sides of the bundle caused by an accumulation of two-phase mixture there [9]. The 1D model predicted $G_{\min}$ = 32.7 kg/m^{2}s, compared to the measured value of 46.9 kg/m^{2}s, 30% low.

Burnside et al. [1] developed a scheme (model A) to include these effects. Model A used video evidence to determine at what row level lateral flow first occurred in individual columns and what was the effective liquid–vapour interface height between bundle and shell. Starting at the centre of the bundle, column 9, the 1D model was applied to each column in turn. It was assumed that the flowrate fell off linearly with height to become zero at the top of the column. Also, the fluid head at the side was made up of liquid up to the assumed liquid/vapour interface level and above that, the gravitational component of the pressure drop at the same level in the column. Proceeding to the 10th column, the same assumptions were made but allowing for lateral inflow of fluid from the centre column and outflow to the

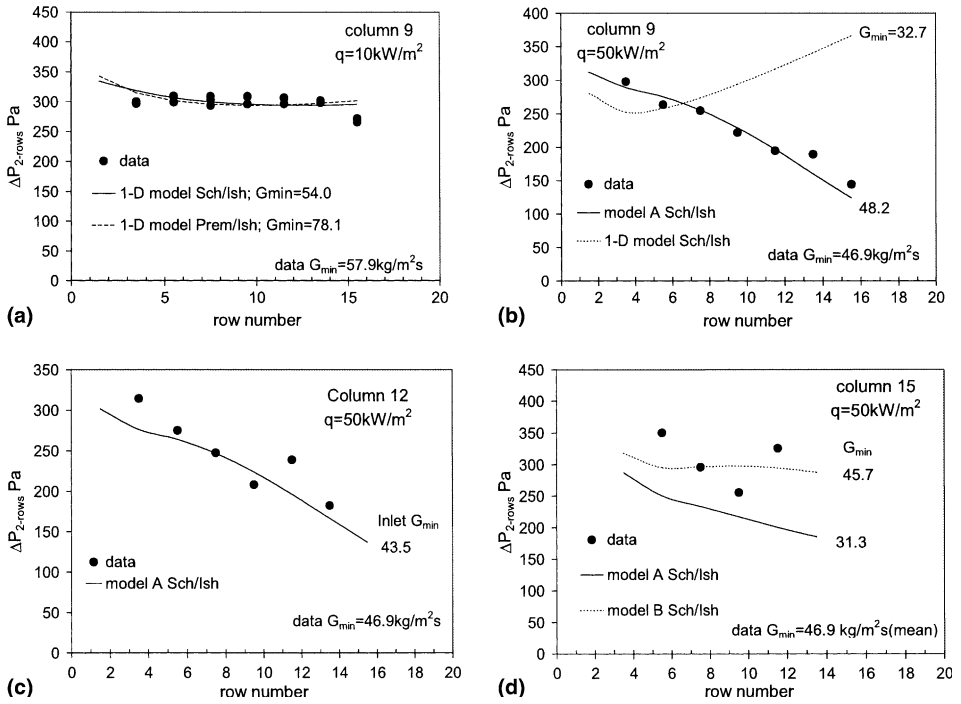

Fig. 15. Measured and predicted mass fluxes and pressure drops. (a) Column 9, $q = 10\,\mathrm{kW/m^2}$; (b) column 9, $q = 50\,\mathrm{kW/m^2}$; (c) column 12, $q = 50\,\mathrm{kW/m^2}$; (d) column 15, $q = 50\,\mathrm{kW/m^2}$.

11th column. The bundle was treated as a collection of square cells, each centered on a tube. The profile of quality in each column, which was affected by both horizontal and vertical flow components, was calculated by applying mass and energy conservation to the flow through the cells. This method was repeated to the edge of the bundle. Excellent agreement was obtained between calculated and measured ΔP in columns 9 and 12 (Fig. 15(b) and (c)). The model A prediction of $G_{\min}$ in column 9 was $48.2\,\mathrm{kg/m^2 s}$ and in column 12, $43.5\,\mathrm{kg/m^2 s}$, compared to the measured value of $46.9\,\mathrm{kg/m^2 s}$, just 3% high and 7% low respectively.

However, model A underpredicted ΔP_{meas} in column 15 by over 30% at the top of the column compared to a least squares fit to the data, (Fig. 15(d)). Further, the mass flux obtained from the PIV measurements was $G_{\min} = 46.9\,\mathrm{kg/m^2 s}$ compared to the model A prediction of $31.3\,\mathrm{kg/m^2 s}$, an underprediction of 33%. On the evidence of the pressure measurements it was argued that the mass flux was not subject to the same constraints in the shorter outside columns as in the centre of the bundle. The momentum imparted by the separation vortex, and the bundle profile at the bottom in the vicinity of the short columns, increased the force balancing the pressure drop due to flow up the columns. This increased the flowrate [1].

To simulate this, model A was modified to treat the mass fluxes, G_{inlet}, entering columns 15–17 as independent variables, together with the fraction of G_{inlet} leaving the top of the columns. This procedure was called model B. As with model A, mass and energy conservation was applied in determining the profiles of quality in the columns. Fig. 15(d) shows the predicted pressure drop in column 15, based on $G_{\mathrm{inlet}} = 50\,\mathrm{kg/m^2 s}$ with 40% of the inlet mass flux assumed to leave at the top. This corresponded to a recirculation mass flux of $45.7\,\mathrm{kg/m^2 s}$, within 3% of the measured value. $\Delta P_{2\text{-rows}}$ was predicted to within 3% of a least squares fit to the data.

The accuracy of these predictions showed that the pressure drop and velocity data were consistent. The value of the velocity measurements in checking the validity of the void fraction correlation is evident. In addition, the velocity vector maps are a valuable platform for 2D CFD studies. It will be recognised that such modelling is necessary to obviate the use of observation of the flow, as required by models A and B.

6. Conclusions

1. PIV measurements can be applied successfully to kettle reboiler configurations. The autocorrelation technique applied caused some difficulties in obtaining vectors, particularly in areas close to the bundle and the separation vortex.

2. Checking and modification of correlations of two-phase flow parameters, as applied to design of kettle reboilers and similar shell and tube heat exchangers, is greatly aided by PIV whole field instantaneous velocity measurements. Further, the measurements are a platform for developing and testing numerical simulations of the flow which can then form the basis of full 3D designs.
3. Pressure drop and mass flux data for pentane, were well predicted by recirculation models based on the Schrage et al. [19] void fraction correlation, although this was developed from air/water and boiling R113 cross-flow data.
4. The recirculatory flow in thin slice laboratory facsimile rigs, suffering inherently from difficulty of phase separation, is time dependent with large amplitude. This factor, as well as any distortion of the flow pattern, must be taken into account when interpreting measurements for design. Effects of this on flow stability are given qualitative consideration above. It is argued that time dependent flow may occur in full size kettle reboilers with high heat fluxes. The primary concern is the estimation of maximum heat flux.

Future research should include:

1. Replacement of the CW laser/rotating mirror/photographic camera PIV acquisition system by a pulsed laser/beam expander/digital cross-correlation camera. Such a set up would reduce troublesome reflections, enlarge the area accesssible to measurement and enhance the dynamic range of the velocity measurements.
2. Extending the field of view as far as possible into bubbly flow areas with seeding of both liquid and vapour.
3. Extending the work to boiling mixtures.

Acknowledgments

The authors are grateful to EPSRC for financial support, GR/L03224 and GR/L03682. Special thanks are due to Alastair Martin for his contribution to establishing the PIV system and to David Walker for his invaluable technical assistance.

References

[1] B.M. Burnside, K.M. Miller, D.A. McNeil, T. Bruce, Heat transfer coefficient distributions in an experimental kettle reboiler thin slice, Trans. IChemE 79 A (2001) 445–452.
[2] R.L. Webb, N.S. Gupte, A critical review of correlations for convective vaporisation in tubes and tube banks, Heat Transfer Eng. 13 (1992) 58–81.
[3] J.W. Palen, C.C. Yang, Circulation boiling model for analysis of kettle and internal reboiler performance, in: Heat Exchangers for 2-phase Applications, ASME Publication HTD 27, 1981, pp. 55–61.
[4] T.W.C. Brisbane, I.D.R. Grant, P.B. Whalley, A prediction method for kettle reboiler performance, ASME Paper No. 80-HT-42, 1980.
[5] N.F. Shire, Heat transfer and hydrodynamics of boiling over tube bundles, Ph.D. Thesis, Heriot-Watt University, 1995.
[6] M.P. King, M.K. Jensen, Local heat transfer and flow pattern distributions in a kettle reboiler, in: Proceedings of the 1st 2-Phase Flow Conference, vol. 2, 1995, pp. 1284–1296.
[7] J.G. Gebbie, M.K. Jensen, Void fraction distributions in a kettle reboiler, Exp. Therm. Fluid Sci. 14 (1997) 297–311.
[8] K.M. Miller, Heat transfer and velocity measurements in a kettle reboiler, Ph.D. Thesis, Heriot-Watt University, 2000.
[9] B.M. Burnside, K.M. Miller, D.A. McNeil, T. Bruce, Pressure drop measurements in a section of a kettle reboiler, 34th National Heat Transfer Conference, Pittsburgh, PA, Paper No. NHTC 2000-12306, CD, ASME, NY, 2000.
[10] B.M. Burnside, K.M. Miller, D.A. McNeil, T. Bruce, Conditions at the outside of a thin slice reboiler bundle determined by particle image velocimetry, in: Proceedings of the 12th International Heat Transfer Conference, vol. 4, 2002, pp. 405–410.
[11] K. Cornwell, N.W. Duffin, R.B. Schuller, An experimental study of the effects of fluid flow on boiling within a kettle reboiler bundle, ASME Publication, 80-HT-45, NY, 1980.
[12] N.F. Shire, B.M. Burnside, R. Didsbury, Circulation velocity measurements in a model multitube reboiler using laser Doppler anemometry, Heat Transfer 1994, in: Proceedings of the 10th International Heat Transfer Conference, vol. 7, pp. 539–544.
[13] L.N. Carlucci, P.F. Galpin, J.D. Brown, Numerical predictions of shellside heat exchanger flows, in: A Reappraisal of Shellside Flow in Heat Exchangers Flows, ASME Publication, HTD-36, 19–26, NY, 1984.
[14] D.P. Edwards, M.K. Jensen, A two-dimensional numerical model of two-phase heat transfer and fluid flow in a kettle reboiler, in: E. Hensel, V.K. Dhir, R. Grief, J. Fillo (Eds.), Phase Change Heat Transfer, HTD 159, vol. 9–16 ASME, New York, 1991.
[15] F.M. Rahman, J.G. Gebbie, M.K. Jensen, An interfacial friction correlation for shell-side vertical 2-phase cross-flow past horizontal in-line and staggered tube bundles, Int. J. Multiphase Flow 22 (1996) 753–766.
[16] B.M. Burnside, 2-D kettle reboiler circulation model, Int. J. Heat Fluid Flow 20 (4) (1999) 437–445.
[17] D.A. McNeil, B.M. Burnside, K.M. Miller, A.H. Tarrad, A comparison between Highflux and plain tubes, boiling pentane in a horizontal kettle reboiler, Appl. Therm. Eng. 22 (2002) 803–814.

[18] M. Raffel, C.E. Willert, J. Kompenhans, Particle Image Velocimetry: A Practical Guide, Springer, Berlin, 1998.
[19] D.S. Schrage, J.-T. Hsu, M.K. Jensen, Two-phase pressure drop in vertical cross-flow across a horizontal tube bundle, AIChE. J. 34 (1) (1988) 107–115.
[20] P.B. Whalley, Boiling, Condensation and Gas–Liquid Flow, Oxford Science Publications, Oxford, 1987.
[21] K. Ishihara, J.W. Palen, J. Taborek, Critical review of correlations for predicting two-phase pressure drop across tube banks, Heat Transfer Eng. 1 (1980) 23–32.
[22] ESDU 1973. Convective heat transfer during cross-flow of fluids over plain tube banks, Item no. 73031, Engineering Science Data Unit, London.